Biosensors and Bioelectronics 132 (2019) 196–202

Contents lists available at ScienceDirect

Biosensors and Bioelectronics

journal homepage: www.elsevier.com/locate/bios

Short communication

Photonic crystal and plasmonic nanohole based label-free biodetection

Arif E. Cetin[a,*], Seda Nur Topkaya[b]

[a] Izmir Biomedicine and Genome Center, 35340 Balcova, Izmir, Turkey
[b] Department of Analytical Chemistry, Faculty of Pharmacy, Izmir Katip Celebi University, Izmir, Turkey

ARTICLE INFO

Keywords:
Photonic crystal
Plasmonics
Nanohole array
Label-free biosensing
Nanofabrication

ABSTRACT

Photonic crystals and plasmonic nanohole arrays are the conventional substrates for label-free biodetection applications. In this article, we readdressed these systems in terms of their sensing capability and provided a broad picture for a selection mechanism of optimum parameters providing strong sensing signals. We first investigated the physical origin of the transmission resonances supported by the two systems, which is the core of the label-free sensing mechanism, relying on strong light-matter interactions. We conducted an extensive theoretical study on optical and sensing properties of the two systems, e.g., linewidth of the optical modes, refractive index sensitivity and figure-of-merit capacities. Our theoretical analyses provided a rule-of-thumb method for the selection of geometrical device parameters of the two systems. In order to experimentally investigate the sensing properties, we fabricated the two systems via a lift-off free fabrication method based on electron beam lithography, where the plasmonic nanohole arrays are realized by covering the phonic crystal surface with a thin metal. As an example, we demonstrated the sensing strength of two systems with identical dimensions by monitoring the spectral variations within their optical responses. We also performed label-free sensing experiments through detection of protein mono- and bilayers, where the geometrical parameters favor the plasmonic sensor system. Integrating a high-resolution optical read-out scheme with a multi-spectral data tracking technique, we achieved an experimentally minimum detectable protein concentration as low as 200 pg/mL for the plasmonic nanohole array and 1 ng/mL for the photonic crystal–based sensing platform.

1. Introduction

Thanks to their extraordinary optical properties, optical biosensor platforms became very essential in fundamental pharmacology and biology research, while very practical and provided accurate data, improving public health by preventing diseases to be pandemic. These optical platforms possess crucial features making them a key asset in the market. In that sense, optical biosensors could provide ultra-sensitive optical responses, accurately distinguishing minute changes within bimolecular interactions (Donath, 2009; Hendry et al., 2010; Ji, 2017). Real-time optical biosensors could also reveal the bimolecular binding kinetics (Massad-Ivanir et al., 2016; Narang et al., 2018). Detection of wide range of biomolecules can be simultaneously detected by multiplexed and high-throughput optical biosensor platforms (Anker et al., 2008; Pan et al., 2013). Furthermore, providing simplicity and affordability, portable biosensors offer accurate diagnosis for resource-poor settings (Lee et al., 2017; Wang et al., 2017).

Recently, label-free optical biosensors have received significant attention as they eliminated the problems related to optical labels, i.e., cost and complexity of the labelling processes, the mismatch between number of labels and the targeted analytes or photo-bleaching (Piliarik and Sandoghdar, 2014). Employing label-free biosensors and signal transduction techniques, platforms with ultra-low detection limits have been shown (Erickson et al., 2007). In the past two decades, label-free optical biosensors employing nano-features have been implemented to achieve ultra-sensitive biosensing, i.e., photonic crystals (Chow et al., 2004; Huang et al., 2009; Shi et al., 2008; Skivesen et al., 2007), and plasmonic nano-apertures or antennas (Chen et al., 2015; Elbahri et al., 2018; Punj et al., 2013; Wu et al., 2012; Wujcik et al., 2014; Zhu et al., 2018). Between different designs, platforms utilizing nanoholes are very popular due to their extraordinary optical properties, which enable to generate strong biosensing signals.

In this article, we investigated the sensing properties of two biosensor platforms, e.g., nanohole based photonic crystals (PCs) and plasmonic nanohole arrays (PNAs). Our main goal is to provide a rule-of-thumb method to choose the optimum geometrical device parameters for PC and PNA systems, and compare their optical and sensing performances for different scenarios. We theoretically investigated the physical origin of the transmission responses of two systems through finite-difference time-domain (FDTD) analyses. We theoretically

* Corresponding author.
E-mail address: arifengin.cetin@ibg.edu.tr (A.E. Cetin).

https://doi.org/10.1016/j.bios.2019.02.047
Received 4 January 2019; Received in revised form 14 February 2019; Accepted 25 February 2019
Available online 27 February 2019
0956-5663/

studied the optical and sensing capacities of the two systems, e.g., spectral linewidth, refractive index sensitivity and figure-of-merit for different dimensions. We showed that each system supports stronger sensing capabilities compared to the other one for each parameter. In addition to the extensive theoretical study, we also experimentally demonstrated the sensing properties of the two systems with identical geometrical parameters for a scenario, where these parameters favor the PNA over the PC system. The realization of the two systems has been done through a lift-off free fabrication method, where the PNA system is realized by simply adding a final step of metal deposition on top of the PC system. We first performed refractive index sensing experiments for bulk solutions to show their sensitivity capabilities in bulk level. We also performed label-free detection of protein mono- and bilayers with these systems, highlighting their applicability in biosensing applications. In order to further improve the sensitivity of these label-free biodetection platforms, we utilized a multi-spectrometer system with an ultra-high spectral resolution and a data-processing technique, where the spectral variations in multiple wavelengths are simultaneously monitored. Using these ultra-sensitive biodetection platforms, we showed an experimental limit-of-detection for protein concentrations, as low as, 200 pg/mL for the plasmonic nanohole array and 1 ng/mL for the photonic crystal biosensor.

2. Materials and methods

Fig. 1A and B show the calculated (grey curve) and the experimental (red curve) transmission responses of the PC and PNA systems with the same hole radius (r = 120 nm), periodicity (a = 600 nm) and dielectric thickness (100 nm). The thickness of the gold film in PNA system is 150 nm and the thickness of the dielectric film (silicon nitride) for both systems is 100 nm. In FDTD simulations, the dielectric constants of gold and titanium were taken from (Palik, 1985). The permittivity of silicon nitride (SiN), 4.67, was determined by ellipsometry. In simulations, in the unit cell consisting of a single nanohole, periodic boundary condition is used along the *x*- and *y*-directions to create the collective periodic aperture behavior and perfectly matched layer boundary condition is used along the propagation direction, *z*. In all directions, the chosen mesh size is 0.5 nm. In the simulations, the polarization of the incident light source is along the *x*-direction. Optical characterization of PC and PNA systems has been performed by visible-near infrared spectroscopy measurements. In the experimental setup, we used an unpolarized halogen lamp since the nanoholes are symmetric in all direction, eliminating the need for a linear polarizer. The light transmitted from PC and PNA chips was collected by a 40 × Zeiss objective lens with NA: 0.65 embedded in an Axio Observer 7 microscope, fiber coupled to an AvaSpec Multichannel Spectrometer. In order to eliminate the effect of the spectral shape of the halogen light source on determining the linewidth of the optical modes supported by the PNA system, the transmission spectra were determined by taking the ratio between the spectra of the transmitted light from the chip and the bare light source, while the background signal is subtracted from both. On the other hand, for the PC system, the light transmitted from the SiN membrane is subtracted from the total transmission to eliminate the incident light contribution.

The figure demonstrates the excellent correlation between simulation and experimental results. The normally incident plane wave source excites the eigenmodes of the system. Accordingly, the PC system has two modes in the visible range locating at 631.5 nm (the second order mode) and 807.3 nm (the first order mode) when the structure is in air. Fig. 1C – left shows the electric field intensity distribution at the top SiN surface. Here, the system has 2-fold symmetry at the lattice along the polarization direction and the local electromagnetic fields are well

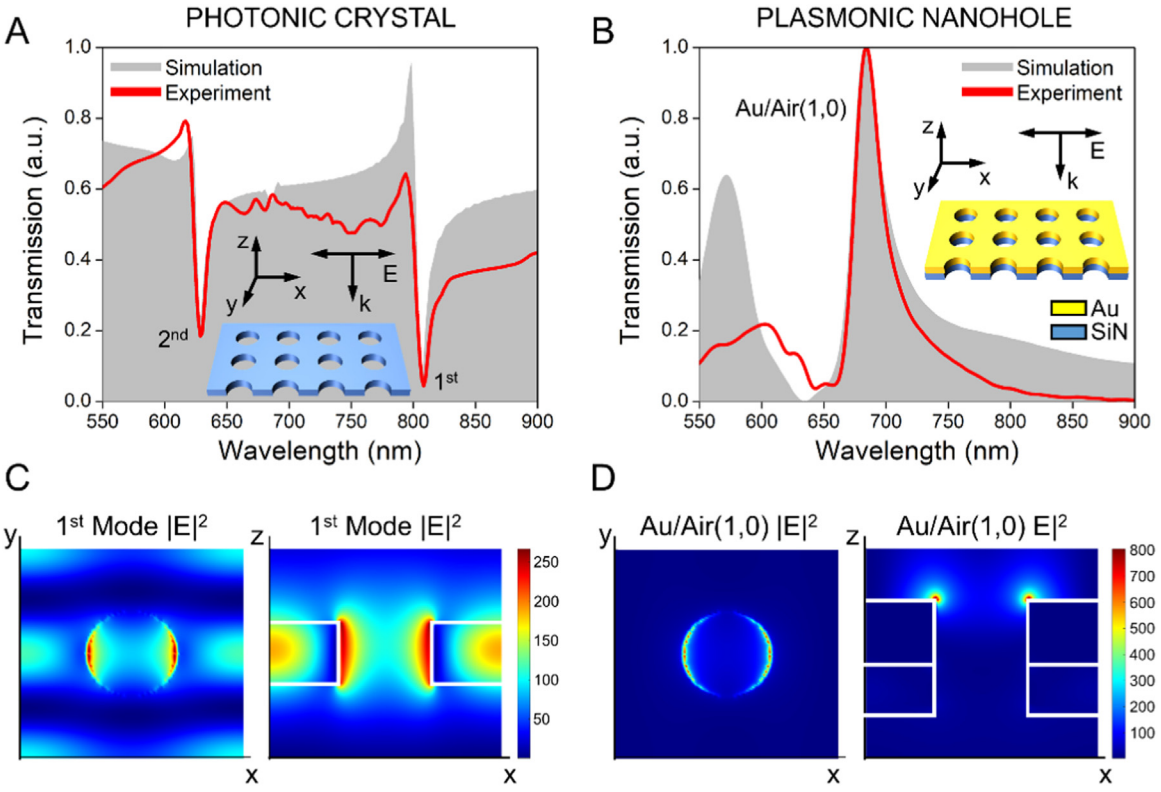

Fig. 1. Calculated (grey) and experimental (red) transmission responses of (A) PC and (B) PNA systems of identical dimensions. Polarization and propagation directions of the incident light source are indicated in the figure insets. The first and second order modes of the PC and Au/Air(1,0) mode of the PNA system are denoted in the figures. (C) Electric field intensity distribution at the top SiN surface and along the cross-section for the PC system. (D) Electric field intensity distribution at the top gold surface and along the cross-section for the PNA system. The corresponding device parameters are: hole radius = 120 nm, array periodicity = 600 nm, thicknesses of SiN and gold layers are 100 nm and 150 nm, respectively.

confined along the edges (Huang et al., 2009). The cross-sectional field profile (Fig. 1C – right) shows that the nearfield localization is focused within the slab and PC surface, extending into the holes. This is very critical to have maximum overlap between local fields and surrounding media (or a biomolecule on the surface) providing higher sensitivities. On the other hand, within the same spectral window, the PNA system supports a single plasmonic mode, arising due to the Au/Air(1,0) mode. The electric field intensity distribution calculated at the top gold surface shows the dipolar character of the mode, concentrating at the two edges of the hole along the polarization direction (Fig. 1D – left). The symmetric standing field pattern observed in the magnetic field intensity distribution (not shown here) shows that the mode arises due to 2 counter-propagating surface plasmons (SPs) (Artar et al., 2009). More importantly, the confined local electromagnetic fields at the top gold surface (Fig. 1D – right) extend deep into the medium in the vicinity, which dramatically increases the sensitivity to the local refractive index changes (Cetin et al., 2015). This is due to the surface wave nature of SPs, i.e., propagating along the gold surface while decaying along the direction normal to it. Here, the tail of these evanescent waves extends into the medium in the vicinity. Therefore, this highly confined field increases the sensitivity to the local refractive index changes as it strengthens the interaction between light and matter in nanometer scale, making the biomolecules significantly alter the properties of light (Ekgasit et al., 2004).

Employing PCs, electromagnetic fields could be spatially extended and light-matter interaction could be enhanced by increasing their overlap. Here, the mode under investigation is the guided mode that is confined within the holes and extends extensively along the vertical direction. The periodic index contrast of the PC configuration enables the excitation of the mode even with a normally incident plane wave source (Huang et al., 2009). Similarly, in PNA systems, the grating order (or the periodicity) overcomes the momentum mismatch between free-space photon and SPs, allowing SP excitation even at normal incidence (Ebbesen et al., 1998). These collinear configurations of PC and PNA systems enable biodetection through much simpler optical setups that are not sensitive to the alignment of source and chip, eliminating prism, waveguide or fiber coupling schemes (Armani et al., 2007; Chana et al., 2001; Mandal and Erickson, 2008; Nedelkov and Nelson, 2003). This configuration could be also very advantageous for biosensing applications, i.e. the targeted analytes on the sensing surface could be simply detected by tracking the variations within the spectrum of the light transmitted from the PC or PNA systems by a spectrometer (Cetin et al., 2017; Huang et al., 2009). Excitation of transmission resonance with normal incidence also makes this configuration very compatible with imaging devices within an array format, dramatically increases the throughput (Chang et al., 2011; Yanik et al., 2011).

In order to realize PC and PNA systems, we utilized a lift-off free fabrication method based on electron beam lithography (EBL) (Yanagi et al., 2015). The steps of the fabrication technique are shown in Fig. 2. We started the fabrication process with a 500 μm thick silicon wafer coated with 100 nm low pressure chemical vapor deposition (LPCVD) SiN films on both sides. We first created a 750 μm × 750 μm square pattern on the bottom SiN film by photolithography. Then, SiN layers under the developed patterns were removed by dry etching while the photoresist was used as a mask. The chips were then immersed in KOH etching to realize free-standing SiN membranes. We performed EBL on a positive resist (Polymethyl methacrylate, PMMA) coated on the top SiN surface. After development, we realized nanoholes through the SiN film via dry etching. We then removed the remaining EBL resist by oxygen plasma cleaning that realizes the PC system. Finally, we deposited 5 nm titanium (adhesion layer) and 150 nm gold, realizing the PNA system. The fabricated PC and PNA systems are shown in scanning electron microscopy (SEM) images in Fig. 2 – inset.

Here, as the two nanohole based systems were created along a thin dielectric membrane, it is very critical to choose a material, making sure that the lab-on-a-chip platforms based on these systems can be reliably used in label-free biosensing applications. Here, LPCVD SiN has large mechanical strength that provides a robust ground. More importantly, the thickness of the SiN membrane is optically transparent, allowing transmission measurements for both PC and PNA systems (Cetin et al., 2017; Huang et al., 2009). In addition, the high refractive index of SiN completes photonic band-gap for the PC system (Paivasaari et al., 2007). On the other hand, for the PNA system, this high refractive index eliminates the SP excitations (in other words, pushes it from the visible and near-IR ranges to much longer wavelengths), existing along the interface between dielectric and metal layer that could result in multiple transmission resonances, spectral distortions or overlaps of transmission resonances in the presence of biomolecules (Cetin et al., 2015).

3. Result and discussion

In this article, our main goal is to provide a rule-of-thumb method for choosing the best parameters for PC and PNA systems yielding strong sensing signals. As we showed in the following section, the geometrical device parameters providing the strongest sensing signals for each system are different, e.g., for the same periodicity, the radius providing the largest sensitivity is different for PC and PNA systems. Bearing this fact in mind, in this section, we showed (not with the aim of comparison) the refractive index sensing capabilities of PC and PNA systems with the same geometrical parameters since the PNA system can be realized simply by a metal deposition on top of the PC surface.

For the transmission resonances supported by PC and PNA systems, the local electromagnetic fields extend extensively within the medium in the vicinity, i.e., they are very sensitive to changes in the local refractive index. In this section, we experimentally investigated the sensing capabilities of the two systems of identical geometrical dimensions by monitoring the spectral variations within the first order mode of the PC system and Au/Air(1,0) mode of the PNA system after immersing them into bulk solutions with different refractive indices, e.g., deionized water (n = 1.33), acetone (n = 1.35), ethanol (n = 1.36) and isopropyl alcohol (IPA, n = 1.37). For both systems, we measured the transmission resonances for different bulk solutions, and determined a linear relationship between resonance wavelengths of the transmission resonances and the refractive indices. Fig. 3A and B show the spectral locations of the transmission resonances supported by the first order mode of the PC and Au/Air(1,0) mode of the PNA system, respectively for different refractive indices of bulk solutions. Here, the slope of the linear curve accounts for the refractive index sensitivity, $S = \Delta\lambda/\Delta n$ (Jackman et al., 2016; Yanik et al., 2010). PC and PNA systems, with r = 100 nm and a = 600 nm, support sensitivities, as large as, 283 and 573 nm/RIU (refractive index unit), respectively. The main reason between these sensitivity values is the local electromagnetic fields with larger intensities supported by the PNA compared to the PC system, i.e., confining larger nearfields on the sensing surface that create a stronger overlap between surface waves and the medium in the vicinity. PC and PNA systems support transmission resonances with linewidths (full-width half-maximum, FWHM), as narrow as, 13.4 and 30.7 nm, respectively. Here, the main difference between linewidths arises due to the metal losses in the PNA system, broadening the plasmonic excitations. Furthermore, supporting spectrally sharp transmission resonances, PC and PNA systems have figure-of-merit (FOM = S/FWHM) values (Li et al., 2015), as large as, 21.1 and 18.7, respectively. These sensitivity and figure-of-merit values are very advantageous for refractive-index sensing based label-free biodetection applications.

In order to further show the sensing properties of the two systems, we investigated linewidth, refractive index sensitivity and figure-of-merit profiles for different hole radius. For the array periodicity of 600 nm, we monitored the hole radius from 60 to 240 nm. For both systems, transmittance of the modes at radius 60 and 90 nm are very low, e.g. they were excluded from the analyses. For the PNA systems with radiuses larger than 150 nm, Au/Air(1,0) mode is distorted as the

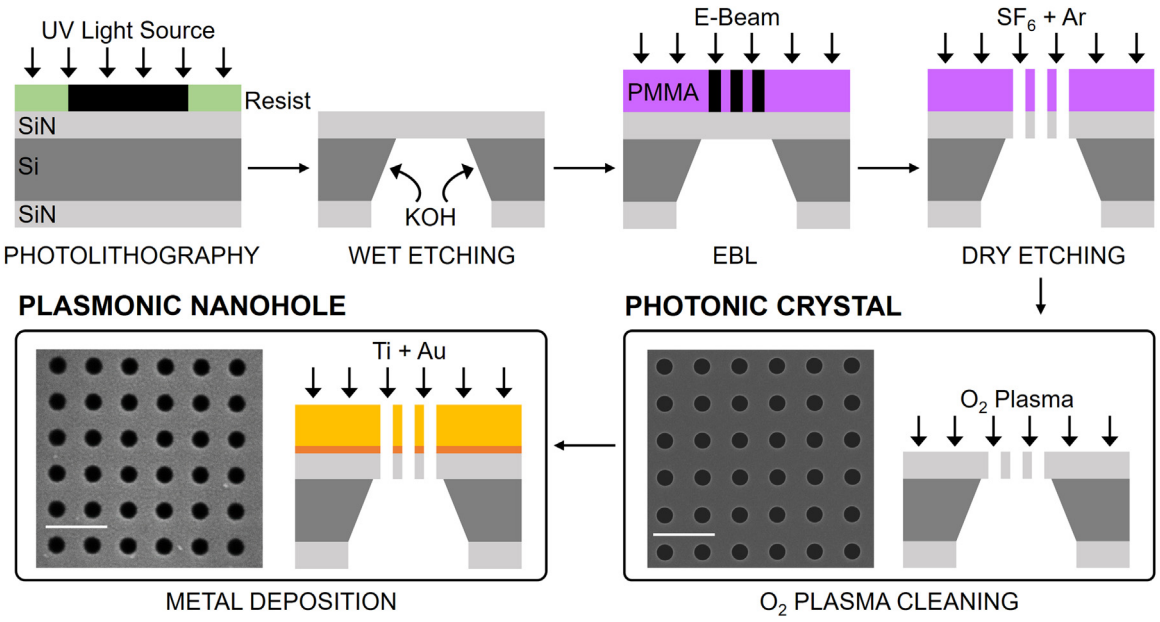

Fig. 2. Schematics of the steps of the nano-fabrication technique for realizing PC and PNA systems. Figure insets show the SEM images of the fabricated PC and PNA systems. Scale: 1 μm. The corresponding device parameters are: hole radius = 120 nm, array periodicity = 600 nm, thicknesses of SiN and gold layers are 100 nm and 150 nm, respectively.

plasmonic nanoholes started to lose its filtering properties, allowing more photons in different wavelengths passing through. Therefore, they were also excluded from the analyses. As shown in Fig. 4A, the transmission resonances shift to shorter wavelengths for PC system since increasing radius lowering band gap frequency in Bragg condition (Yablonovitch, 1993). For the PNA system in Fig. 4B, the transmission resonances shift to longer wavelengths since the cavity modes have a linear relationship with the length (in this case, the diameter or radius of the holes) (Adato et al., 2009). For both systems, the linewidth of the transmission resonances increases due to the widening of the spectral window of the photons passing through the subwavelength holes (Fig. 4C and D). Fig. 4E and F show that the refractive index sensitivity of the transmission resonances supported by the PC system increases, while the one supported by the PNA system decreases. As the rate of the increase in the linewidth of the transmission resonances is larger than that of in the refractive index sensitivity, FOM decreases for the PC system with larger radiuses (Fig. 4G). On the other hand, decreasing sensitivity and increasing linewidth with radius further decrease FOM for the PNA system with larger hole radiuses (Fig. 4H).

In order to experimentally compare the sensitivity capabilities of the two systems with the same dimensions, we performed label-free detection of protein mono- and bilayers (Cetin et al., 2014a, 2014b; Coskun et al., 2014). Here, we used a protein bilayer composed of protein A/G and protein IgG. Before the surface functionalization, the chip surface was cleaned with a piranha solution (H_2SO_4: H_2O_2 = 3: 1) in order to dissipate any biochemical contamination on the surface. We formed the monolayer by immobilizing 100 μg/mL protein A/G on the chip surface, followed by a PBS (phosphate buffered saline) rinse to remove the unbound proteins. Protein A/G, which is a recombinant fusion of proteins A and G with a ~50 kDa molecular weight, binds on

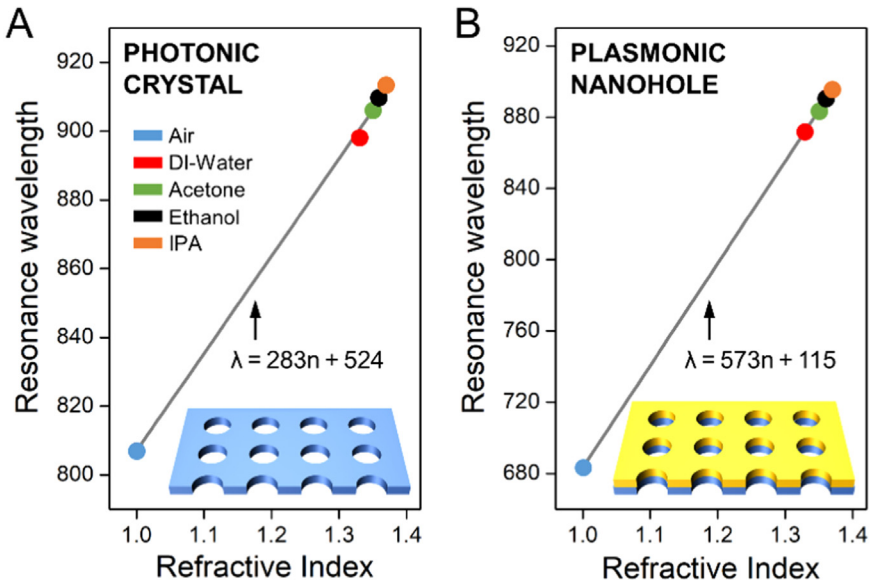

Fig. 3. Spectral variations within the transmission resonances supported by (A) the first order mode of the PC and (B) Au/Air(1,0) mode of the PNA system. The corresponding device parameters are: hole radius = 120 nm, array periodicity = 600 nm, thicknesses of SiN and gold layers are 100 nm and 150 nm, respectively.

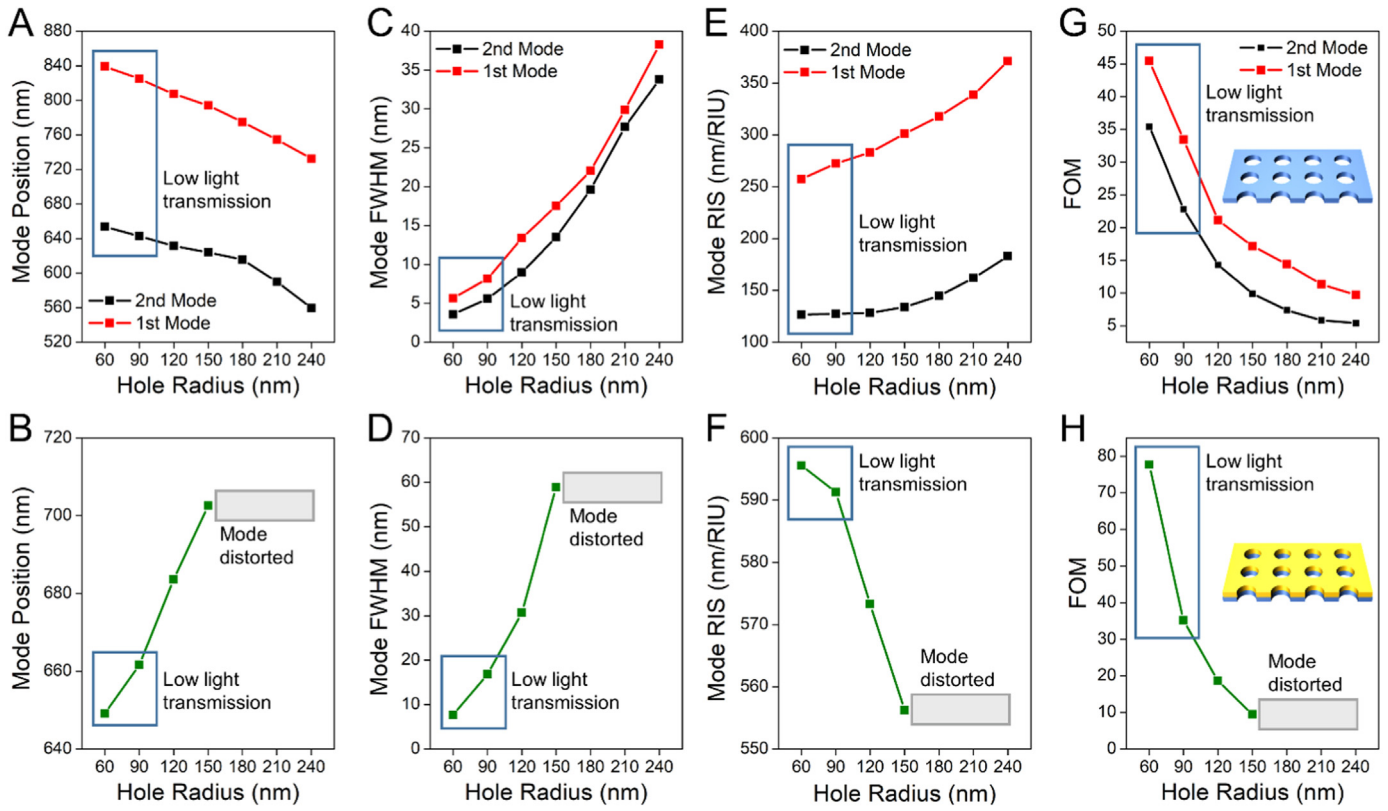

Fig. 4. Variations within the spectral location of the transmission resonance maxima for (A) PC and (B) PNA systems. Variations within the linewidth (FWHM) of the transmission resonances supported by (C) PC and (D) PNA systems. Variations within the refractive index sensitivity (RIS) of (E) PC and (F) PNA systems. Variations within the figure-of-merit (FOM) of the transmission resonances supported by (G) PC and (H) PNA systems. The corresponding device parameters are: array periodicity = 600 nm, thicknesses of SiN and gold layers are 100 nm and 150 nm, respectively.

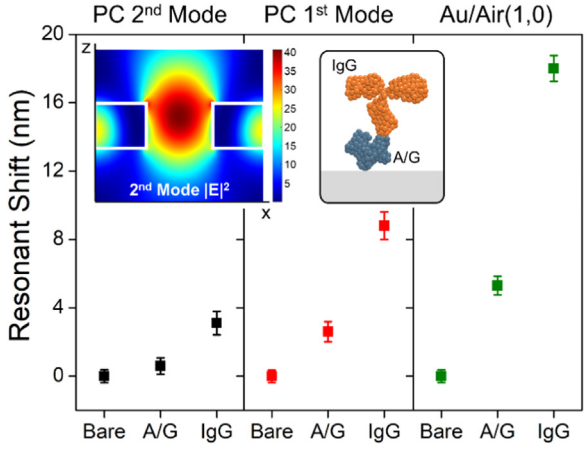

Fig. 5. Spectral variations within the transmission resonances supported by PC (black: the second order, red: the first order) and PNA systems (green: Au/Air (1,0) mode) upon the attachment of 100 μg/mL protein A/G and 100 μg/mL protein IgG. Figure inset – left: Cross-sectional electric field intensity distribution for the second order mode of the PC system. Figure inset – right: Protein IgG standing on A/G through its Fc region, forming a "Y" shape on the sensing surface. The corresponding device parameters are: hole radius = 120 nm, array periodicity = 600 nm, thicknesses of SiN and gold layers are 100 nm and 150 nm, respectively.

the gold surface by physisorption. We then functionalized 100 μg/mL protein IgG on the A/G coated chip surface followed by PBS rinsing. Protein IgG was captured on the sensing surface due to the high affinity of protein A/G to the Fc regions of protein IgG, i.e., IgG stands on the gold surface, forming a "Y" shape (Fig. 5 – inset: The schematics shows the protein IgG sticking on A/G along its Fc region). The molecular weight of protein IgG is ~150 kDa. Here, we used such high protein concentrations to make sure that we saturated the protein amount on the sensing surface, i.e., we can reliably compare the sensing properties of PC and PNA systems. Fig. 5 shows the spectral shift amounts observed within the transmission resonances supported by the PC (black: the second order mode, red: the first order mode) and the PNA systems (green: Au/Air(1,0) mode) after the addition of protein mono- and bilayers. The figure shows the mean values with error bars (twice the standard deviation from three independent experiments). As the current geometrical configuration is more favorable for the PNA system, Au/Air (1,0) mode shifts by 5.3 nm and 18 nm after the addition of protein mono- and bilayers, respectively. On the other hand, for the PC system, the first (second) order mode shifts by 2.6 (0.6) nm and 8.8 (3.1) nm after the addition of protein mono- and bilayers, respectively. Here, we observed the smallest spectral shift for the second order mode of the PC system since for this mode, the local electromagnetic fields squeezed within the holes were more than 5 times weaker than that of the first order mode (Fig. 5 – inset shows the cross-sectional electric field intensity profile for the second order mode), resulting in a weaker spatial overlap between light and targeted biomolecules (Cetin et al., 2014a, 2014b).

To further demonstrate the sensing capabilities of the two systems, we performed label-free detection of a wide range of IgG concentrations, from 0.1 ng/mL to 100 μg/mL. For such small protein amounts, the classical approach, e.g., monitoring the resonance wavelength of the optical modes, fails as it relies only on spectral data at a single wavelength (Cetin et al., 2015). Instead, monitoring spectral variations in multiple wavelengths could further lower the limit of detection (LOD) (Lee and Wei, 2010; Stewart et al., 2006). In order to consider the spectral variations around the transmission resonances supported

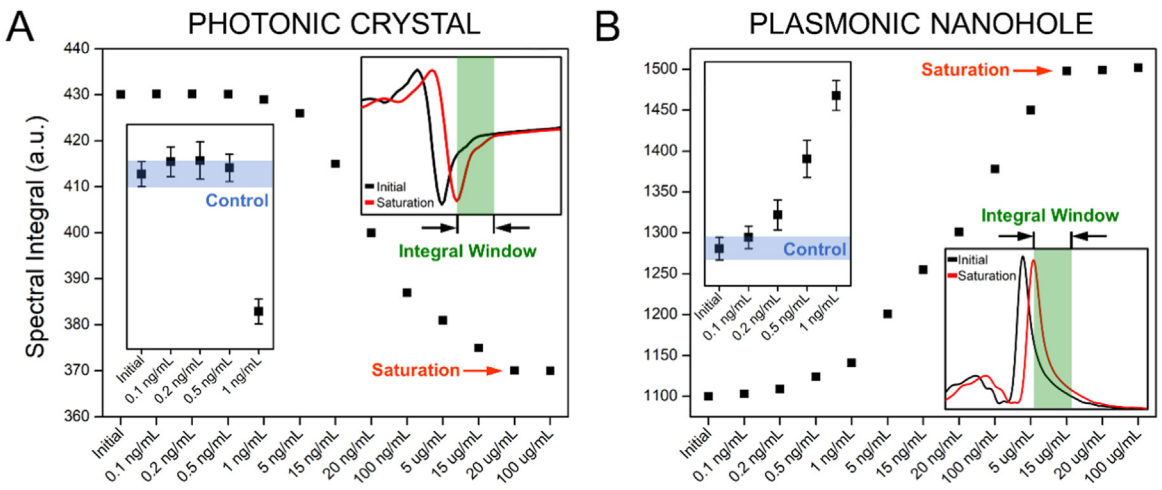

Fig. 6. Spectral integral values calculated for IgG concentrations from 0.1 ng/mL to 100 μg/mL for (A) PC and (B) PNA systems. Figure insets on the right: Transmission resonances before the IgG attachment (black curves) and after the attachment of 100 μg/mL IgG (red curves), which ensures the surface saturation. In the spectral integral method, the transmission values are summed in the spectral windows highlighted with green boxes. Figure insets on the left: Spectral integral values for 4 different IgG concentrations in a zoomed figure. LOD of each system is highlighted with a blue box, defined by the mean values of the transmission responses before the IgG attachment and twice the standard deviation from 3 independent experiments. The protein concentrations for surface saturation are highlighted with red arrows. The corresponding device parameters are: hole radius = 120 nm, array periodicity = 600 nm, thicknesses of SiN and gold layers are 100 nm and 150 nm, respectively.

by the two systems, we defined a spectral window where we integrated the light transmission, highlighted with the green boxes in the insets on the right in Fig. 6A and B (PC: ~818 nm to ~840 nm, PNA: ~702 nm to ~778 nm). Fig. 6A and B show the spectral integral values for different IgG concentrations captured at PC and PNA surfaces, respectively. Here, we determined the resonance wavelength of the first order mode of the PC system and Au/Air(1,0) mode of the PNA system (red curves in the insets on the right), where their surfaces are saturated with a high IgG concentration, i.e., 100 μg/mL. Then, we defined a spectral window, starting from these resonance wavelengths of the saturation condition, and possessing the wavelengths, where the transmission behaviors are well-defined and free of any spectral distortions. This approach eliminates any unexpected variations in the spectral integral values due to an unwanted transmission peak or dip. We also smoothened the transmission resonances with Savitzky–Golay filter in order to eliminate any contributions from the noise of the spectrometer. Here, we scanned the visible and near-IR range with a high spectral resolution, e.g., 0.9 Å, though a multiple-spectrometer system (dividing the spectral range of interest by multiple spectrometers working simultaneously to increase the resolution). As the IgG concentrations increase, transmission resonances shift to longer wavelengths, i.e., for the PC system, spectral integral value decreases, whereas it increases for the PNA system. For both systems, the protein concentrations for the surface saturation (no spectral variation observed after these points), e.g., 20 μg/mL for PC and 15 μg/mL for PNA, are highlighted with red arrows. In order to experimentally demonstrate the minimum detectable IgG concentration by the two systems, we performed 3 independent experiments for the IgG concentrations between 0.1 ng/mL to 1 ng/mL. The figure insets on the left show the mean values of the spectral integral values with error bars calculated by adding twice the standard deviation from the three independent experiments (Cetin et al., 2014a, 2014b, 2015). Here, LOD has been determined by the initial transmission response of the PC or PNA chip before the IgG attachment, in other words, the transmission response of the chips covered with protein A/G, as denoted with the blue boxes in the figure insets on the left. For the PNA and PC systems, the minimum reliably and experimentally detectable IgG concentrations are found as 0.2 ng/mL and 1 ng/mL, respectively. These LOD values are very critical for bimolecular interactions of ultra-low protein concentrations. More importantly, integrating this spectral evaluation technique to a high-resolution spectrometer based read-out mechanism and an ultra-sensitive PC or PNA chip, sensitivity of the label-free biosensors could be reduced to the SPR working regimes, where a typical commercial SPR platform has an LOD on the order of 10 pg/mL (Nguyen et al., 2015).

4. Conclusions

In conclusion, in this article we investigated the sensing properties of two conventional biosensing substrates, nanohole based photonic crystals and plasmonic nanohole arrays. We theoretically investigated the physical origin of the transmission resonances supported by the two systems and provided a fine-tuning mechanism of their spectral positions, leading to strong sensing signals. We theoretically studied the dependence of the linewidth of the transmission resonances, refractive index sensitivity and the figure-of-merit profiles of both systems on the geometrical device parameters. We also manufactured the photonic crystal and plasmonic nanohole array systems with identical dimensions via a lift-off free fabrication technique based on electron beam lithography. We performed sensing experiments with bulk solutions to demonstrate refractive index sensing capabilities of both systems. Finally, we performed label-free sensing of protein mono- and bilayers. Utilizing a spectral integral method, where the spectral variations at different wavelengths can be simultaneously evaluated, we showed a limit-of-detection as low as 1 ng/mL and 200 pg/mL, for photonic crystal and plasmonic nanohole array based biosensor system, respectively. We believe the work conducted in this article will provide a rule-of-thumb method for selecting geometrical parameters for nanohole based photonic crystal and plasmonic biodetection platforms providing very strong sensing signals. Furthermore, employing a powerful spectral evaluation technique and a high-resolution spectrometer integrated to an ultra-sensitive PC or PNA chip, sensitivity of label-free biosensors could be reduced to the SPR working regimes in the future.

CRediT authorship contribution statement

Arif E. Cetin: Conceptualization, Data curation, Formal analysis, Writing - original draft, Writing - review & editing, Software, Validation, Investigation. **Seda Nur Topkaya:** Formal analysis, Writing - original draft, Writing - review & editing, Investigation, Methodology.

Acknowledgements

A.E.C. acknowledges Izmir Biomedicine and Genome Center Start-Up Research Grant.

Declaration of interests

None.

References

Adato, R., Yanik, A.A., Amsden, J.J., Kaplan, D.L., Omenetto, F.G., Hong, M.K., Erramilli, S., Altug, H., 2009. Proc. Natl. Acad. Sci. USA 106, 19227.
Anker, J.N., Hall, W.P., Lyandres, O., Shah, N.C., Zhao, J., Van Duyne, R.P., 2008. Nat. Mater. 7, 442.
Armani, A.M., Kulkarni, R.P., Fraser, S.E., Flagan, R.C., Vahala, K.J., 2007. Science 317, 783.
Artar, A., Yanik, A.A., Altug, H., 2009. Appl. Phys. Lett. 95, 051105.
Cetin, A.E., Coskun, A.F., Galarreta, B.C., Huang, M., Herman, D., Ozcan, A., Altug, H., 2014a. Light Sci. Appl. 3, e122.
Cetin, A.E., Drsata, M., Eksioglu, Y., Petracek, J., 2017. Plasmonics 12, 655.
Cetin, A.E., Etezadi, D., Altug, H., 2014b. Adv. Opt. Mater. 2, 866.
Cetin, A.E., Etezadi, D., Galarreta, B., Busson, M.P., Eksioglu, Y., Altug, H., 2015. ACS Photonics 2, 1167.
Chana, S., Li, Y., Rothberg, L.J., Miller, B.L., Fauchet, P.M., 2001. Mater. Sci. Eng. C 15, 277.
Chang, T.Y., Huang, M., Yanik, A.A., Tsai, H.Y., Shi, P., Aksu, S., Yanik, M.F., Altug, H., 2011. Lab Chip 11, 3596.
Chen, X., Ciraci, C., Smith, D.R., Oh, S.H., 2015. Nano Lett. 15, 107.
Chow, E., Grot, A., Mirkarimi, L.W., Sigalas, M., Girolami, G., 2004. Opt. Lett. 29, 1093.
Coskun, A.F., Cetin, A.E., Galarreta, B.C., Alvarez, D.A., Altug, H., Ozcan, A., 2014. Sci. Rep. 4, 6789.
Donath, E., 2009. Nat. Nanotechnol. 4, 215–216.
Ebbesen, T.W., Lezec, H.J., Ghaemi, H.F., Thio, T., Wolff, P.A., 1998. Nature 391, 667.
Ekgasit, S., Thammacharoen, C., Yu, F., Knoll, W., 2004. Anal. Chem. 76, 2210.
Elbahri, M., Abdelaziz, M., Homaeigohar, S., Elsharawy, A., Hedayati, M.K., Roder, C., Assad, M.E.H., Abdelaziz, R., 2018. Adv. Mater. 30, 1704442.
Erickson, D., Mandal, S., Yang, A.H.J., Cordovez, B., 2007. Microfluid. Nanofluid. 4, 33.
Hendry, E., Carpy, T., Johnston, J., Popland, M., Mikhaylovskiy, R.V., Lapthorn, A.J., Kelly, S.M., Barron, L.D., Gadegaard, N., Kadodwala, M., 2010. Nat. Nanotechnol. 5, 783–787.
Huang, M., Yanik, A.A., Chang, T.Y., Altug, H., 2009. Opt. Express 17, 24224.
Jackman, J.A., Linardy, E., Yoo, D., Seo, J., Ng, W.B., Klemme, D.J., Wittenberg, N.J., Oh, S.H., Cho, N.J., 2016. Small 12, 1159.
Ji, N., 2017. Nat. Methods 14, 374–380.
Lee, K.L., Wei, P.K., 2010. Small 6, 1900.
Lee, W.I., Shrivastava, S., Duy, L.T., Kim, B.Y., Son, Y.M., Lee, N.E., 2017. Biosens. Bioelectron. 94, 643.
Li, J., Ye, J., Chen, C., Li, Y., Verellen, N., Moshchalkov, V.V., Lagae, L., Van Dorpe, P., 2015. ACS Photonics 2, 425.
Mandal, S., Erickson, S., 2008. Opt. Express 16, 1623.
Massad-Ivanir, N., Shtenberg, G., Raz, N., Gazenbeek, C., Budding, D., Bos, M.P., Segal, E., 2016. Sci. Rep. 6, 38099.
Narang, R., Mohammadi, S., Ashani, M.M., Sadabadi, H., Hejazi, H., Zarifi, M.H., Sanati-Nezhad, A., 2018. Sci. Rep. 8, 15807.
Nedelkov, D., Nelson, R.W., 2003. Trends Biotechnol. 21, 301.
Nguyen, H.H., Park, J., Kang, S., Kim, M., 2015. Sensors 15, 10481.
Paivasaari, K., Tikhomirov, V.K., Turunen, J., 2007. Opt. Express 15, 2336.
Palik, E.D., 1985. Handbook of Optical Constants of Solids. Academic, Orlando.
Pan, J., Zhang, H., Cha, T.G., Chen, H., Choi, J.H., 2013. Anal. Chem. 85, 8391.
Piliarik, M., Sandoghdar, V., 2014. Nat. Commun. 5, 4495.
Punj, D., Mivelle, M., Moparthi, S.B., van Zanten, T.S., Rigneault, H., van Hulst, N.F., Garcia-Parajo, M.F., Wenger, J., 2013. Nat. Nanotechnol. 8, 512.
Shi, L., Pottier, P., Peter, Y.A., Skorobogatiy, M., 2008. Opt. Express 16, 17962.
Skivesen, N., Tetu, A., Kristensen, M., Kjems, J., Frandsen, L.H., Borel, P.I., 2007. Opt. Express 15, 3169.
Stewart, M.E., Mack, N.H., Malyarchuk, V., Soares, J.A.N.T., Lee, T.W., Gray, S.K., Nuzzo, R.G., Rogers, J.A., 2006. Proc. Natl. Acad. Sci. USA 103, 17143.
Wang, L.J., Chang, Y.C., Sun, R., Li, L., 2017. Biosens. Bioelectron. 87, 686.
Wu, C., Khanikaev, A.B., Adato, R., Arju, N., Yanik, A.A., Altug, H., Shvets, G., 2012. Nat. Mater. 11, 69.
Wujcik, E.K., Wei, H., Zhang, X., Guo, J., Yan, X., Sutrave, N., Wei, S., Guo, Z., 2014. RSC Adv. 4, 43725.
Yablonovitch, E., 1993. J. Phys. Condens. Matter 5, 2443.
Yanagi, I., Ishida, T., Fujisaki, K., Takeda, K., 2015. Sci. Rep. 5, 14656.
Yanik, A.A., Cetin, A.E., Huang, M., Artar, A., Mousavi, S.H., Khanikaev, A., Connor, J.H., Shvets, G., Altug, H., 2011. Proc. Natl. Acad. Sci. USA 108, 11784.
Yanik, A.A., Huang, M., Artar, A., Chang, T.Y., Altug, H., 2010. Appl. Phys. Lett. 96, 021101.
Zhu, Y., Li, Z., Hao, Z., DiMarco, C., Maturavongsadit, P., Hao, Y., Lu, M., Stein, A., Wang, Q., Hone, J., Yu, N., Lin, Q., 2018. Light. Sci. Appl. 7, 67.